Available online at www.sciencedirect.com
ScienceDirect
Computers & Fluids 36 (2007) 1621–1637
computers & fluids
www.elsevier.com/locate/compfluid

On a mechanism of stabilizing turbulent free shear layers in cavity flows ☆

Michael J. Stanek [a,*], Miguel R. Visbal [a], Donald P. Rizzetta [a], Stanley G Rubin [b], Prem K. Khosla [b]

[a] *Air Force Research Laboratory, Wright-Patterson AFB, OH, United States*
[b] *University of Cincinnati, Cincinnati, OH, United States*

Available online 30 March 2007

Abstract

Turbulent free shear flows are subject to the well-known Kelvin–Helmholtz type [Panton RL. Incompressible flow. John Wiley and Sons; 1984. p. 675] instability, and it is well-known that any free shear flow which approximates a thin vorticity layer will be unstable to a wide range of amplitudes and frequencies of disturbance. In fact, much of what constitutes flow control in turbulent free shear layers consists of feeding a prescribed destabilizing disturbance to these layers. The question in the control of free shear flows is not whether the shear layer will be stable, but whether you can influence *how* the layer becomes unstable. In most cases, since these flows are so receptive to forcing input, and naturally tend toward instability, large changes in flow conditions can be achieved with very small amplitude periodic inputs.

Recently, it has been discovered that turbulent free shear flows can also be stabilized using periodic forcing. This is, at first glance, counter-intuitive, considering our long history of considering these flows to be very unstable to forcing input. It is a phenomenon not described in modern fluid dynamic text books. The forcing required to achieve this effect (which we will call turbulent shear layer stabilization) is of a much higher amplitude and frequency than the more traditional type of shear layer flow control effect seen in the literature (which we will call turbulent shear layer destabilization).

A numerical study is undertaken to investigate the effect of frequency of pulsed mass injection on the nature of stabilization, destabilization and acoustic suppression in high speed cavity flows. An implicit, 2nd-order in space and time flow solver, coupled with a recently developed hybrid RANS-LES (Reynolds Averaged Navier Stokes-Large Eddy Simulation) turbulence model by Nichols and Nelson [Nichols RH, Nelson CC. Weapons bay acoustic predictions using a multi-scale turbulence model. In: Proceedings of the ITEA 2001 aircraft-stores compatibility symposium, March 2001], is utilized in a Chimera-based parallel format. This tool is used to numerically simulate both an unsuppressed cavity in resonance, as well as the effect of mass-addition pulsed jet flow control on cavity flow physics and ultimately, cavity acoustic levels.

Frequency (and in a limited number of cases, amplitude) of pulse is varied, from 0 Hz (steady) up to 5000 Hz. The change in the character of the flow control effect as pulsing frequency is changed is described, and linked to changes in acoustic levels. Limited comparison to 1/10th scale experiments is presented.

The observed local stabilization of the cavity turbulent shear layer, when subjected to high frequency pulsed blowing, is shown in simulation to be the result of a violent instability and breakdown of a pair of opposite sign vortical structures created with each high frequency ''pulse''. This unique shear layer stabilization behavior is only observed in simulation above a certain critical pulsing frequency. Below this critical frequency, pulsing is shown in simulation to provide little benefit with respect to suppression of high cavity acoustic levels.
© 2007 Published by Elsevier Ltd.

☆ This paper is declared a work of the US Government and is not subject to copyright protection in the United States. Approved for public release. Distribution unlimited.

* Corresponding author.
E-mail address: Michael.Stanek@wpafb.af.mil (M.J. Stanek).

0045-7930/$ - see front matter © 2007 Published by Elsevier Ltd.
doi:10.1016/j.compfluid.2007.03.011

1. Introduction

The high speed flow past an open cavity (such as the flow past an open weapons bay on a bomber or fighter aircraft) is capable of generating a type of acoustic resonance, which can produce very high acoustic levels. This type of flow is driven and dominated by the Kelvin–Helmholtz type [1] instability of the free shear layer which starts at the front edge of the cavity, and terminates at the downstream trailing edge of the cavity. Large-scale coherent vortical structures are present in these types of resonant free shear flows. Passive leading edge spoiler devices are routinely applied in modern aircraft with weapons bays in an effort to reduce damaging acoustic levels, but these devices are only of limited effectiveness over a relatively narrow parameter range of aircraft operation.

Research in active or powered pulsed flow control to suppress acoustic resonance in cavities began to appear in cavity applications in the early 1990s, presumably in response to the popularity of modern flow control in other applications. A comprehensive recent review of active flow control applied to the cavity problem is provided in Cattafesta et al. [3]. Modern open-loop flow control (without use of controllers or feedback) applied to cavities has been divided into three distinct categories, namely, zero frequency, low frequency (LF), and high frequency (HF). This natural division was created based upon observed differences in experiments in the effect of different types of flow control schemes [4]. In the current work, all three of these types of open-loop control were simulated, and a working definition of the boundary between low frequency and high frequency control will be offered later in the discussion. Experimental high frequency control has been demonstrated at frequencies a factor of 10 higher than the dominant natural cavity modes – the current work shows significant benefit at frequencies a factor of 3 higher.

The first successful application of HF pulsed flow control in a subsonic cavity (Mach = 0.6) was reported by McGrath and Shaw [5] in 1996. The first successful supersonic cavity (Mach = 1.2) suppression experiment using HF pulsing was reported by Stanek et al. [6] in 2000. In that test, two HF pulsing devices, a rod in crossflow, and a massflow powered pulsating resonance tube device, provided significantly better suppression than a passive spoiler. Subsequent cavity testing cast doubt on whether suppression with the resonance tubes was due to "pulsing effects" [7] (jets with and without pulsing provided the same suppression benefit), while confirming that the effective suppression of the HF "shedding rod" device was in fact due to HF pulsing [8].

Stanek et al. [4] reviewed open-loop active and passive flow control techniques applied to high speed cavities in 2001. They found that any effective control in the LF pulsing range due to active flow control was limited to Mach numbers below the range of interest for practical military applications ($.8 < \text{Mach} < 1.5$). Inside this practical range of Mach numbers, the only techniques which were effective and provided some reasonable acoustic suppression (on the order of 10 dB reduction of acoustic levels) were passive spoilers, jets (pulsing or steady), and rods in crossflow (shedding HF pulsating vorticity). For LF pulsing jets, no significant additional benefit was found to be provided due to the pulsing. The *only* devices which exceeded the suppression performance of passive spoilers in high speed cavities were high massflow jets, and HF pulsing rods in crossflow (a zero-mass-flow-addition device).

The impressive experimental success of the new HF flow control devices (rods and possibly pulsed jets) in cavities led to attempts to model these devices computationally. Four high-fidelity simulations of HF pulsed flow control in cavities have been reported in the literature, all relying on LES type resolution in the cavity region. Rizzetta and Visbal [9] simulated the effect of a 5 kHz pulsed jet ahead of a Mach 1.19 cavity. The calculation with and without HF flow control was performed using an LES formulation at a Reynolds number based on cavity length of 200,000 (or $Re/ft = 120{,}000$). Arunajatesan et al. [10] simulated the effect of a rod in crossflow (which sheds vorticity at HF) submerged in the shear layer ahead of a Mach 0.6 cavity flow. The shedding frequency of the rod was not reported. That calculation, with and without flow control, was performed using a hybrid RANS-LES formulation, at a Reynolds number per unit length of 1.45 million. Tramel et al. [11] also simulated the effect of a rod in crossflow actuator, on a cavity embedded in the side of a transport aircraft (at Mach.85), and in a generic cavity configuration (at Mach.95). Das et al. [12] compared steady mass injection to HF pulsed mass injection, in the same cavity configuration as Rizzetta and Visbal [9], except at a higher Reynolds number (Reynolds number based on cavity length of 1,000,000). Das et al. [12] used a DES type formulation, and showed a slight improvement (about 3 dB) in 2nd Rossiter mode suppression on the rear wall, using pulsed injection over steady injection.

Most of the aforementioned simulation-based studies demonstrated significant acoustic suppression after the application of HF flow control, but did not offer a compelling argument as to the nature of the suppression mechanism. The difficulty lies in the fact that all of these simulations described a characteristic of the unsteady cavity after suppression (such as turbulent kinetic energy dissipation rate, turbulent kinetic energy production rate, etc.), but not the sequence of events which led up to that state. In other words, they adequately described the characteristics of the patients' state (dead, heart not beating, riger mortis, etc.), but did not describe the chain of events which led the patient to change state (patient gets angry, gets in fight, takes bullet in chest, etc.).

The intention behind the current work was to study through simulation, a range of frequencies of pulsing, to help illuminate the root cause of acoustic suppression in the experimental cavity cases using HF pulsing – to show what changes as you move from low frequencies (where pulsing is ineffective) to high frequencies (where pulsing is

effective). In this way, the "switch" from LF control to HF control could be captured and defined – and an effective boundary between the two regimes (and an explanation for that boundary) could be developed. This is the first time that such an explanation has been presented in the literature.

This comprehensive study made an efficient and accurate solution procedure a requirement, and dictated the use of some type of combined RANS-LES technique. The aim was to capture essential features of the Rizzetta and Visbal [9] LES with and without pulsing, but in a much shorter time frame using fewer resources than the Rizzetta and Visbal [9] LES. The Rizzetta and Visbal [9] simulation parameters were used as an ad hoc benchmark to gauge the relative savings of the approach used in the current investigation. In addition, the intention was to expand the investigation to much higher Reynolds numbers, and to study a much broader range of pulsing frequency than the Rizzetta et al. cavity simulation.

The Rizzetta and Visbal [9] simulation used approximately 20 million grid points, to simulate the cavity flow experiment described in Stanek et al. [6], but at a reduced Reynolds number. The non-dimensional timestep used in Rizzetta and Visbal [9] was approximately .0005, which works out to approximately 300 timesteps per cycle of pulsing (at 5 kHz). The rough goal for the present work was to simulate the same case, at the actual Reynolds number of the experiment, on a grid of about 3–5 million points. The goal for the timestep was to be able to run accurate and stable solutions at the same timestep as Rizzetta and Visbal [9].

This approach has demonstrated that it can yield useful solutions at a Reynolds number a factor of 36 higher than the Rizzetta and Visbal [9] simulation, at one quarter the computational cost (for the cavity solution). The savings are increased further, when one considers the additional expense required to compute the LES inflow boundary-layer solution, used to provide the unsteady input conditions to the Rizzetta and Visbal [9] calculation. In the case of the present work, these savings translate directly into increased number of cases in the computational matrix.

In the process, this numerical approach also captured descriptions of relevant physical phenomenon consistent with all available experimental cavity results which used HF pulsed flow control devices, and helped provide key evidence of the chain of events responsible for the effect.

1.1. Flow solver

The same flow solver (FDL3DI [13]) described in the Rizzetta and Visbal [9] LES calculation was used in the current cavity simulations. In preliminary cavity calculations the use of 4th-order spacial differencing was considered. After it was discovered that 2nd-order spacial accuracy offered sufficient spacial resolution and superior numerical stability characteristics, the same solver used in Rizzetta and Visbal [9], with 2nd-order spacial accuracy, was retained for the remainder of the study.

2. Governing equations

The governing equations used for the current simulations are the unsteady, three-dimensional, mass-averaged, full Navier–Stokes equations, written in non-dimensional, strong-conservation form [14], using a general, time-dependent coordinate transformation ξ, η, ζ, t:

$$\frac{\partial Q}{\partial t}+\frac{\partial}{\partial \xi}\left(F-\frac{1}{Re}F_{\mathrm{v}}\right)+\frac{\partial}{\partial \eta}\left(G-\frac{1}{Re}G_{\mathrm{v}}\right)+\frac{\partial}{\partial \zeta}\left(H-\frac{1}{Re}H_{\mathrm{v}}\right) \tag{1}$$

Here, Q is the vector of dependent variables, F, G, H the inviscid flux vectors, and F_{v}, G_{v}, H_{v} the viscous flux vectors. A detailed description of the governing equations can be found in Ref. [15] and is not duplicated here.

The system of equations is closed using the perfect gas law, Sutherland's formula for viscosity, and the assumption of a constant molecular and turbulent Prandtl number, $Pr = 0.72$, and $Pr_{\mathrm{t}} = 0.9$. Flow quantities have been non-dimensionalized by freestream values except for pressure, which is non-dimensionalized by the freestream dynamic pressure, $\rho_\infty u_\infty^2$. All lengths have been normalized by the length of the cavity, measured from leading edge to trailing edge. The Boussinesq eddy viscosity approximation is employed to model the Reynolds stresses. A turbulence model is used to obtain values for the eddy viscosity – it will be described in a subsequent section.

3. Boundary conditions

Fig. 1 shows the major grid structure/topology, and Fig. 2 shows a schematic of the cavity, indicating the relative location of the pulsed flow control boundary condition.

Both a course and fine grid were used in the present study. Upstream inflow boundary conditions were applied in one of two different ways. For baseline cases on the

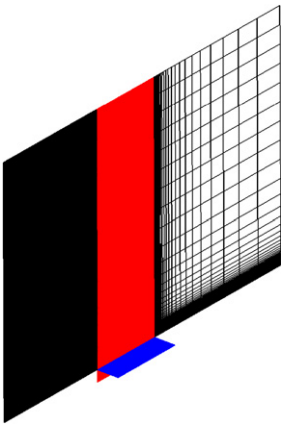

Fig. 1. Grid structure showing main computational regions.

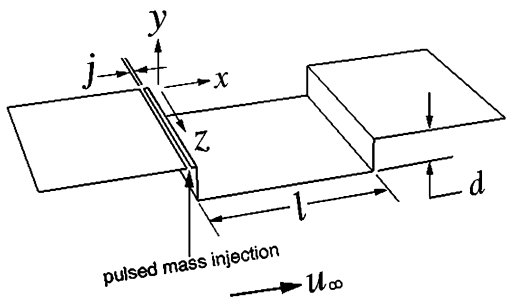

Fig. 2. Schematic of cavity configuration showing location of pulsing boundary condition.

course grid without flow control, a shortened inflow section was used, and inflow properties were obtained from a separate turbulent flat-plate boundary-layer calculation. For all cases on the fine grid (with and without flow control), the full extent of the flat-plate leading edge region in the experiment [6] is used, including the leading edge. At the inflow plane (five planes ahead of the leading edge), free-stream properties are imposed.

At the remaining outer boundaries, first-order extrapolation of the interior flow values is used. On the solid surfaces (cavity, inflow plate, outflow plate), a no-slip condition is applied, along with the assumption of an adiabatic wall, and a zero normal pressure derivative. In the spanwise (z) direction, periodicity was assumed, and a standard five plane overlap was used to obtain boundary conditions. This overlap allows for the evaluation of a 4th-order central spacial differencing at the last computed point (for numerical damping) without a change in the differencing stencil. Boundary conditions for the pulsed blowing slot will be discussed in the section on flow control results. Boundary conditions for the k–ε equations used for the turbulence modeling will be discussed in the next section.

4. Numerical procedure

The governing equations are solved numerically using the implicit, approximately factored algorithm of Beam and Warming [16]. The equations are discretized using 2nd-order Euler implicit time differencing and 2nd-order accurate central differences for all spacial derivatives. A blend of second and 4th-order nonlinear dissipation per the suggestion of Jameson et al. [17] is used to stabilize the central-difference scheme. The diagonal form of the Beam-Warming algorithm developed by Pulliam and Chaussee [18] has been implemented in the solver and used on this problem. Temporal accuracy, which can be degraded by use of the diagonal form, is maintained by utilizing subiterations within a time step [19]. This technique reduces errors due to factorization, linearization, and explicit application of boundary conditions. The technique is useful for maintaining temporal accuracy on overset zonal mesh systems, and for domain decomposition implemented on parallel computers. The subiteration technique is also useful for enhancing accuracy in the application of the two-equation turbulence model, which is uncoupled from the main flow equations during a subiteration, but "loosely coupled" with the flow equations over a timestep. The solutions in the current study use three subiterations for each timestep.

The features of the numerical algorithm described above have been implemented in a parallel version of the time-accurate three-dimensional computer code FDL3DI [13]. This code has been validated on a wide range of steady and unsteady flows (both laminar and turbulent), including vortical flows over delta wings [19–22], vortex breakdown [20–22], direct numerical simulation (DNS) of transitional wall jets [23], synthetic jet actuators [24], and DNS and LES of subsonic [25] and supersonic flow-fields [26,27], including supersonic cavity flow [9].

5. Turbulence model

The hybrid RANS-LES model of Nichols and Nelson [2,28] is used to account for the effects of small scale turbulence downstream of the cavity leading edge, and uses a standard k–ε two-equation model as part of its formulation. The same k–ε model is used throughout the solution domain (with or without the hybrid RANS-LES treatment), and will be described below first.

The two-equation k–ε model developed by Jones and Launder [29] for the solution of incompressible boundary-layer flows is used in the current cavity studies. The Jones and Launder low-Reynolds number terms are included to provide for improved near wall modeling and ease in applying the wall boundary conditions for k and ε. The complete set of k–ε equations are included in Ref. [15].

This two-equation turbulence model was integrated into the previously described Navier–Stokes computer code by Rizzetta [30]. The k–ε equations are solved with a numerical procedure identical to that used for the Navier–Stokes equations, and are loosely coupled with the Navier–Stokes equation set through the subiteration process within a timestep.

The basic idea behind all the hybrid RANS-LES models is the notion that grid densities in modern calculations in certain regions can become fine enough to capture at least part of the range of applicable turbulent scales. The assumption inherent in traditional turbulence models is that the effect of *all* of the turbulent scales must be accounted for by the model. This leads to portions of the flowfield being "overdamped", because dissipation is being provided naturally by the flow physics captured in the calculation, as well as by the turbulence model. The hybrid RANS-LES models would seek to sense those regions of sufficient grid density, away from no-slip walls, where this excessive dissipation can be eliminated. The end result is more effective resolution of the local flow-field for a given density of grid.

The hybrid RANS-LES turbulence model employed in the current simulations is the scheme of Nichols and

Nelson [28]. It is described in Nichols and Nelson as a multi-scale (MS) model, in the same tradition as multi-scale models developed by Hanjalic et al. [31], Kim and Chen [32], or Duncan and Liou [33].

A set of strategies for turbulent kinetic energy production limitation, as well as for enhanced numerical stability was employed in this study. Details of those strategies can be found in Ref. [15].

5.1. Boundary conditions

In the hybrid RANS-LES formulation described above, the values of k and ε are non-dimensionalized by u_∞^2 and u_∞^3/L, respectively, where u_∞ is the freestream velocity, and L is the length of the cavity from leading edge to trailing edge.

Freestream values of k and ε are specified at the far field boundaries. The freestream value k_∞ is obtained by defining a freestream turbulence intensity, T_i, as

$$T_i = \left[\frac{2}{3}k_\infty\right]^{\frac{1}{2}} \Big/ u_\infty \tag{2}$$

The value of T_i is assumed to be $T_i = 0.005$. A corresponding value of ε_∞ is then determined by assuming $\mu_{t_\infty} = \mu_\infty$. The values of k and ε are set to zero at the no-slip surfaces. All other boundary conditions on k and ε are specified in a manner similar to that used for the flow variables.

6. Computational details

Fig. 3 shows a close-up view of the fine grid cavity leading edge region. In both the coarse and fine grids, the resolution of the inflow region is the same, and this resolution density was validated using a separate flat-plate turbulent boundary-layer calculation. The difference in this fine grid is in the cavity region, where the spacing is halved (resolution doubled) in both the x and y directions over the coarse. In the z-direction, a slightly reduced span (from .5 to .3) was chosen on the fine grid to enhance resolution in that direction as well. The coarse grid calculations with the hybrid turbulence model (which eliminates unphysical excessive dissipation) produced substantially more (and smaller) scales of vortical structures, and that experience guided the choice of reduced span on the fine grid.

Tables 1 and 2 list the dimensions of the major domains for both 3D grids, as well as the cavity region dimensions in each grid. Table 3 lists key dimensions and spacings for the fine grid, which was used for the bulk of the numerical studies in this study.

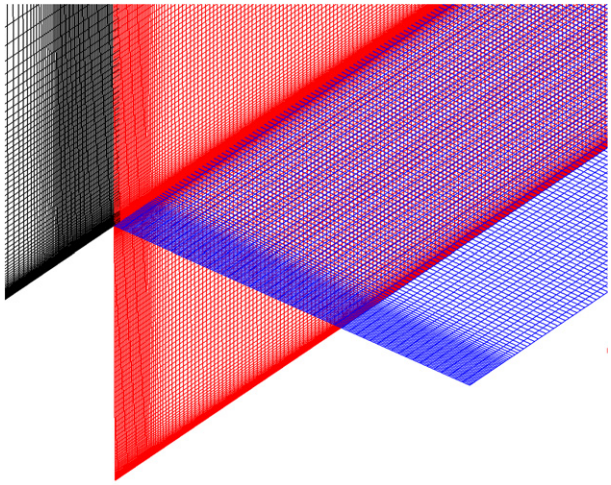

Fig. 3. Fine grid – close-up of cavity leading edge. Spacing in x and y is half that of coarse grid in cavity portion. Note spacing in z is also reduced, due to reduction in z span on this grid.

The Chimera [34,35] domain decomposition methodology was utilized in the current numerical simulations. This methodology allows the entire computational flowfield to be partitioned into a number of less complex overlapping or embedded regions for which grids may be easily constructed. In the present simulations, three main domains are defined (inflow, mid-region, outflow) as shown in Fig. 1. To enable solution on a parallel computer, each of these three main domains was further subdivided into smaller computational regions.

The entire computational mesh was decomposed into 19 separate domains, using Chimera [34,35] domain decomposition methodology. Each separate partition was distributed on an individual processor of a parallel computing platform (Compaq SC-40/45). The decomposition was designed to provide an approximately equal number of grid points in each domain, to balance the work load among the computational processors. Faces at the boundaries of each block were overset into adjacent domains, such that a mutual overlap of five planes was shared between blocks. All overlapping mesh points were coincident, except for those blocks which bounded the line from the cavity leading edge to the outer boundary. No interpolation was required for the coincident boundary overlapping points. For those points lying along the line from the cavity leading edge to the outer boundary, a 2nd-order interpolation procedure was employed. Automated software was used to identify donor and recipient points [36]. Inter-node communication among the processors was established

Table 1
Three-dimensional grid sizes

Name	Inflow dimensions $I * J * K$	Midsection and cavity $I * J * K$	Outflow dimensions $I * J * K$	Total number of points
Coarse	124 * 129 * 51	232 * 252 * 51	64 * 129 * 51	4,218,516
Fine	147 * 159 * 51	292 * 250 * 51	54 * 101 * 51	5,193,177

Table 2
Cavity section non-dimensional grid lengths

Name	Width	Height	Length
Coarse	0.5	0.2	1.0
Fine	0.3	0.2	1.0

Table 3
X and Y parameters for fine grid

Location	X	ΔX	Y	ΔY
Inflow boundary	−1.633	0.01666	–	–
Cavity leading edge point	0.0	0.001389	0.0	0.000003
Cavity trailing edge point	1.0	0.001389	0.0	0.0001
Outflow boundary	3.22	0.4	–	–
Largest spacing inside of cavity	–	0.004	–	0.004
Cavity ceiling	–	–	0.2	0.0005
Along $Y = 0.0$ line from leading edge to outflow	–	–	0.0	0.0001
Top of domain	–	–	4.109	0.33
Leading edge of flat plate	−1.55	0.01666	–	–
Start of pulsed blowing slot	−.05278	0.00125	–	–
End of pulsed blowing slot	−.02778	0.00125	–	–

using standard message-passing interface (MPI) library routines [37].

A five point overlap is used at computational block interfaces to allow for inter-block boundary conditions. This allows for the evaluation of 4th-order central spacial differencing at the last computed point (for numerical damping) without a change in the differencing stencil.

Several strategies were employed to improve numerical stability and enable reasonable timestep, including maintaining piecewise continuous stretching factor everywhere, biasing the block decomposition in the vicinity of the cavity "waterline", and judicious and sparing use of numerical filtering in selected regions. Details are available in Ref. [15].

7. Baseline computational results

7.1. Numerical validation – grid and timestep studies

In this section, the effects of timestep, grid spacing, extent of the spanwise domain, and turbulence modeling are considered. All simulations were conducted at a Reynolds number based upon cavity length of 7.23 million, and at a Mach number of 1.19.

The overarching strategy of the numerical simulations, was to find the least expensive technique possible which would capture the relevant physics, and then to utilize this technique (and the relative low cost) to study an entire series of cases (not just one or two). Due to the nature of this approach, the "validation" was not expected to achieve grid independent results, but simply to show a steady progression towards the correct behavior as resolution was increased.

In addition, the formal "validation" (with respect to grid or time resolution) is restricted to baseline cases – cases in the absence of flow control.

7.2. Inflow validation

The computation of the incoming boundary layer, required for inflow conditions on the "truncated" coarse grid, gave us the opportunity to verify that the k–ε turbulence model was producing a "proper" turbulent boundary layer.

Fig. 4 shows that the current numerical calculation of turbulent skin friction tracks with a classical turbulent correlation curve. A laminar skin friction correlations is included for comparison.

Fig. 5 shows that we also reproduce the proper turbulent boundary-layer behavior, when we examine a profile just

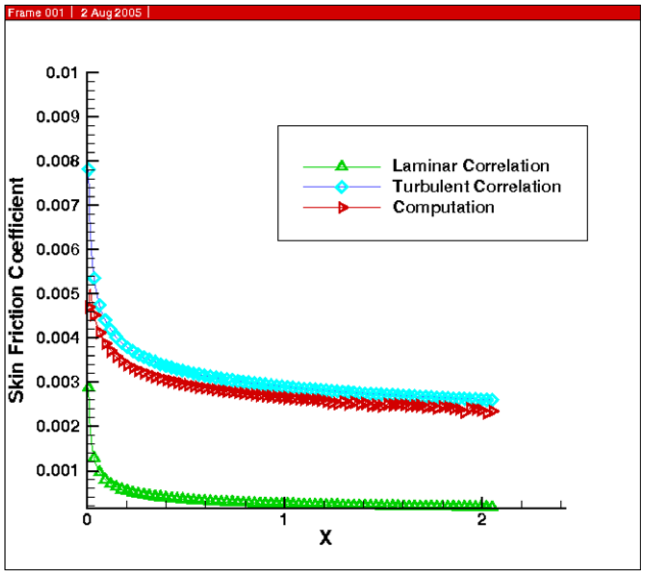

Fig. 4. Skin friction on flat plate vs. X. Validation of turbulent boundary-layer calculation used for inflow profiles.

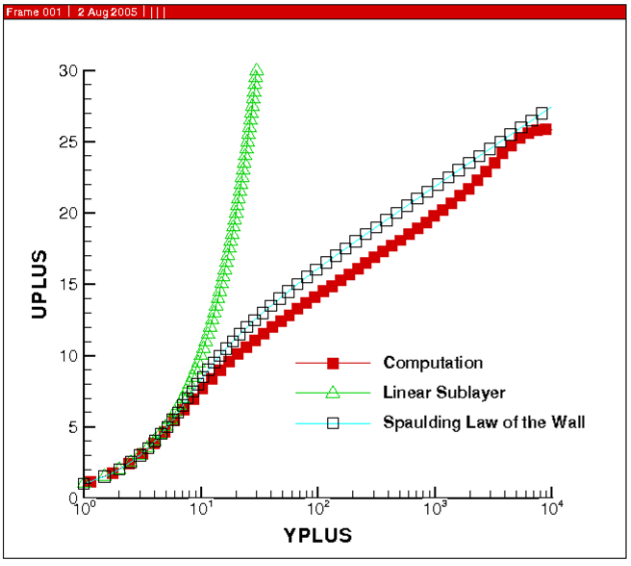

Fig. 5. Boundary-layer profile in wall coordinates, just upstream of cavity leading edge position.

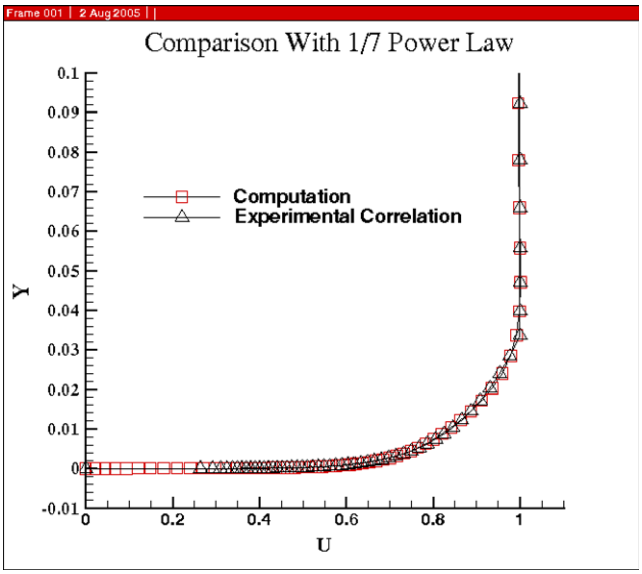

Fig. 6. U velocity profile, compared to classic 1/7 power-law correlation.

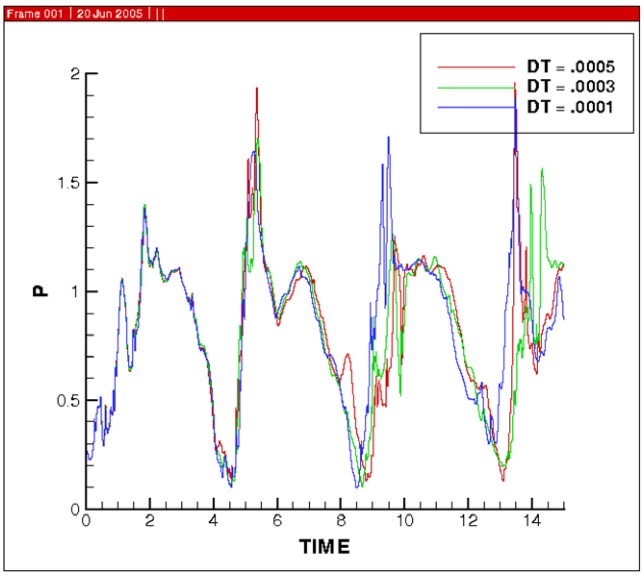

Fig. 7. Effect of varying timestep on unsteady pressure on cavity ceiling near rear wall ($x = 0.9$). Computation on fine grid.

upstream of the cavity leading edge, in terms of the velocity profile in wall coordinates. Finally, Fig. 6 shows that we reproduce the classical 1/7th power law profile when the velocity profile is plotted in those coordinates.

7.3. 2D baseline cavity timestep study

The decision as to choice of timestep was made based partly upon previous experience of Rizzetta and Visbal [9], where they studied the same cavity under the same operating conditions (except at a much lower Reynolds number), using a large-eddy simulation technique. Even though they ran their simulation at a much lower Reynolds number, the comparison is useful because the current simulations use a similar minimum spacing to theirs in the cavity portion of the flowfield. In addition, a brief study was conducted in 2D of the effect of timestep on the solution.

Fig. 7 shows the effect of three different timesteps on the computed pressure history near the rear wall (on the cavity ceiling, at $x = 0.9$). Note that the term "ceiling" is used in the present work to refer to the horizontal wall surface inside the cavity. The cavity rear wall is at $x = 1.0$. The cavity leading edge is at $x = 0.0$. Given that the flow is not strictly periodic (but chaotic with strong tendencies toward periodicity), it is reassuring that the three solutions match as well as they do. They maintain phase with each other for most of the 15 characteristic times of the comparison, and track quite closely with each other for at least 8 of those characteristic times. In the cavity portion of this simulation, the minimum spacing (in x or y since this is 2D) matches that of the simulation of Rizzetta and Visbal [9].

The largest timestep considered corresponds to that of the Rizzetta and Visbal [9] cavity simulation, $dt = .0005$. Based upon the result of this 15 characteristic time run, it was decided to run all future 2D and 3D simulations at the mean non-dimensional timestep considered, $dt = .0003$. This corresponds to roughly 500 timesteps per pulse oscillation (at 5000 Hz), and to approximately 5000 timesteps per oscillation at the dominant 2nd Rossiter cavity mode.

7.4. 3D grid resolution study

The study of grid resolution requirements was extended to 3D. In the process, the dynamic character of the cavity was altered by allowing shear layer instabilities to develop in the z-direction.

Table 4 shows the list of 3D baseline cases, and assigns a name to each case. This shorthand notation will be used in the descriptions that follow. The description begins by first looking at the behavior of the turbulence models on the two 3D grids.

Fig. 8 (inset "a") shows the contours of eddy viscosity produced by the k–ε model for the Base 1 case. In order to get "reasonable" behavior from this model, the allowable value of eddy viscosity was "capped" or limited at each timestep, to some value above that produced in the incoming boundary layer (so as not to affect the incoming boundary layer). Without this cap, the k–ε model produced so much dissipation that the cavity barely sustained any oscillatory behavior at all.

Table 4
List of three-dimensional baseline cavity simulations

Name	Turb. model	Pulse freq. (Hz)	Pulse amp. (V/U_∞)	Steady amp.	Grid
Base 1	k–ε	0.0	0.0	0.0	Coarse
Base 2	Hybrid	0.0	0.0	0.0	Coarse
Base 3	Hybrid	0.0	0.0	0.0	Fine

Fig. 8. Midspan eddy viscosity contours. Top to bottom – (a) coarse grid, k–ε, (b) coarse grid – hybrid, (c) fine grid – hybrid.

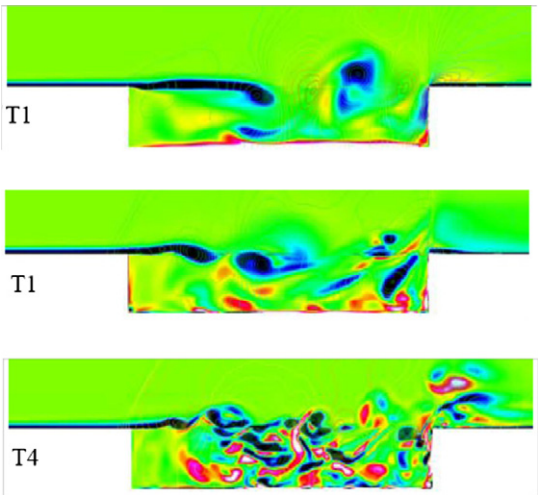

Fig. 9. Z component of vorticity, on midspan. Top to bottom – (a) coarse grid, k–ε, (b) coarse grid -hybrid, (c) fine grid – hybrid.

Due to the fact that there are source terms in the k–ε model equations, the eddy-viscosity tends to accumulate (production is proportional to the local values of eddy viscosity from the last iteration) in the cavity, and the "capping technique" does not eliminate the excessive production. The physics of the problem dictates that the model should only produce turbulence (essentially eddy viscosity) in regions with high levels of vorticity (such as in the cavity shear layer). Fig. 8 (inset "a") shows that high eddy viscosity levels persist everywhere within the cavity in spite of the cap. The reason there is a "white space" to the left of the figure, is that we have chosen to use a common view and scale for all these figures, and the "white space" is where the extended inflow portion of the fine grid case (Base 3 – inset "c") fits.

Fig. 8 (inset "b") shows the effect of turning on the Hybrid RANS-LES model. It is evident now that the excessive levels of eddy viscosity are no longer seen in the cavity, and the production of turbulent kinetic energy (and hence eddy viscosity) is constrained to areas in and around the cavity shear layer.

Finally, it can be seen in Fig. 8 (inset "c"), that production of eddy viscosity in the cavity (relative to values in the wall-bounded shear layers) has been essentially eliminated. This is due to the fact that the fine 3D grid has provided sufficient resolution for the model to revert to large-eddy simulation within the cavity, and little additional turbulent viscous damping is provided by the model. The maximum value of turbulent kinetic energy computed in the cavity region on the fine grid was examined during the use of the hybrid model. It was found that the maximum value naturally "captured" by the grid resolution and the flow equations was 0.3385, compared to apeak value of approximately 0.01 computed by the turbulence model – a factor of 30 times larger. Keep in mind that the eddy viscosity computed from the turbulence model turbulent kinetic energy would be filtered to even lower values (before being fed to the flow equations) after the application of the filtering function in the hybrid model.

Note that the extent of the upstream domain now fills the figure for the fine grid. This is the domain and grid which was chosen for the 3D cavity studies with flow control.

Fig. 9 shows the corresponding effect of increased resolution/improved turbulence model on z component of vorticity contours for Base 1, Base 2, and Base 3 computations.

Fig. 10 shows the ceiling pressure trace ($x = 0.9$) which corresponds to the Base 3 case (fine grid, hybrid model). In Fig. 10, it can be seen that the calculation transitioned from a 1st-mode-dominant behavior to a "mixed" mode behavior at about time = 25. The simulation continued to mature, and another "transition" to dominant 2nd mode oscillation took place at about time = 46. The dominant 2nd mode behavior is confirmed in the $x = 0.9$ ceiling pressure spectra in Fig. 11.

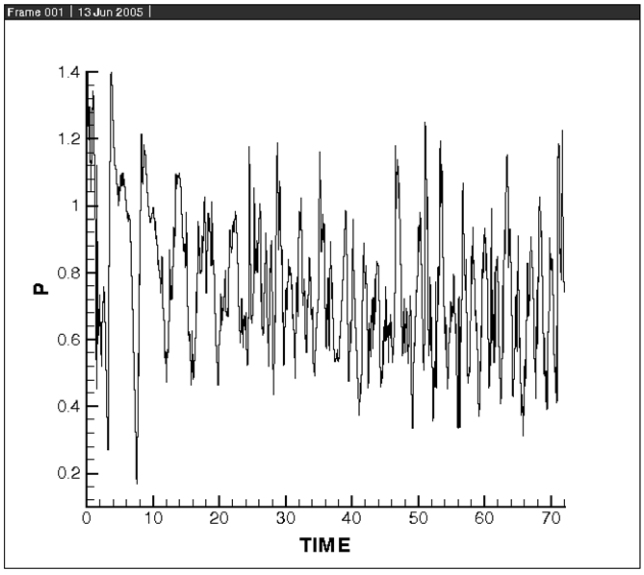

Fig. 10. Base 3, 3D fine grid, hybrid model, pressure trace ($x = 0.9$).

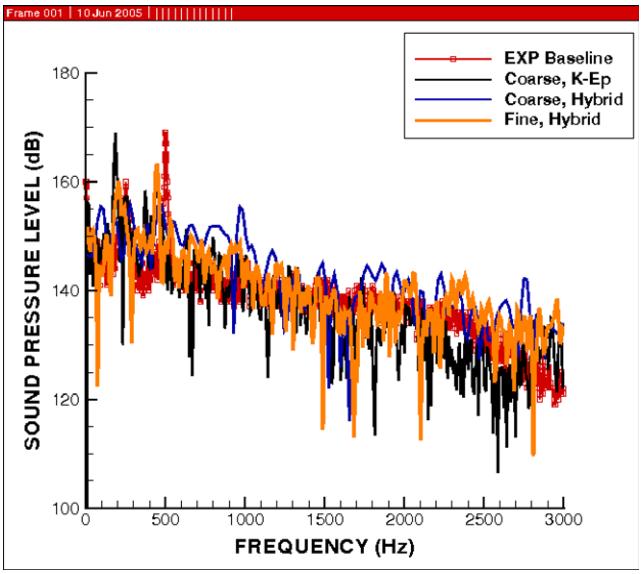

Fig. 11. Ceiling pressure spectra ($x = 0.9$) – all three baseline cases and experimental data.

It can be seen in Fig. 11 that the 1st-mode amplitude is captured quite accurately, and the 2nd mode, while still the dominant tone, is under predicted by approximately 5 dB.

It was believed that the reproduction of the proper Rossiter tones, and the steady progression from dominance of the 1st mode through dominance of the 2nd mode (the proper behavior) as the resolution of the cases was increased was sufficient validation to proceed with the evaluation of flow control techniques on the finest resolution grid.

8. Pulsed blowing flow control

The effect of periodic mass injection through the upstream slot is achieved by specifying the following profile for the non-dimensional velocity, v

$$v = \left[A[\sin(0.5\omega_t)]^2 + A_{\text{steady}}\right] \sin\omega_x \tag{3}$$

$$\omega_x = \pi\left(\frac{x - x_{j1}}{x_{j2} - x_{j1}}\right) \tag{4}$$

$$\omega_t = 2\pi L \times f/u_\infty \tag{5}$$

In the equations above, x_{j1} and x_{j2} are the upstream and downstream extent of the injection slot. For a pure pulsing jet, with no steady injection, the coefficient "A_{steady}" is set to zero in Eq. (3). For a pure steady jet, the coefficient "A" is set to zero. Equivalences between steady mass flow rates and pulsed rates were obtained by writing two expressions for the average jet momentum (one involving constant velocity, and one involving pulsing velocity, integrated over one period of pulse) and equating the two expressions This was used to determine the appropriate pulse amplitude which would replicate the measured experimental flow control mass flow rate.

The form of the pulsing remained the same in 3D as in 2D, due to the assumption of spanwise coherence of the input pulse in the 3D calculations.

8.1. Effect of forcing amplitude

As mentioned previously, the primary intent of 2D pulsing studies was to determine numerical stability of the solution procedure. These studies were all performed on the fine grid. After determining that the appropriate value of "A" in Eq. (3) to match experiment was 1.67, the authors sought to verify that this value could be reached in the simulation. Keep in mind that the value $A = 1.67$ represents a peak slot exit Mach number of 1.99, oscillating at 5000 Hz. Values of "A" of .1, .3, .5, 1.0, 1.5, and 2.0 were attempted, to see what would be possible in the event that 1.67 would prove to be too difficult to achieve. A goal of "A" of 2.0 in 2D simulation was set, to provide some assurance that $A = 1.67$ could be reached when transitioning to 3D solutions.

Solution instability (at the desired timestep of $\Delta t = 0.0003$) was encounter in the vicinity of the wall, just downstream of the ejected mass, for values of "A" greater than 0.5. This numerical oscillation was damped by applying a small "patch" of 2nd-order explicit filtering in the region of concern. After this adjustment, successful simulations up to "A" = 2.0 (at an oscillation frequency of 5000 Hz) were achieved.

8.2. 3D flow control cases

Table 5 lists all the 3D numerical cavity cases, with and without flow control, considered in the current work. Due to "real-world" time constraints, it was not possible to run the Base 3 non-flow-control case to completion before beginning the flow control cases – they had to be run simultaneously. Therefore the starting solution for several of the flow control runs was the Base 3 case at an immature state. This is not considered problematic, because the solution at the time clearly displayed "dominant" 1st and 2nd modes which had to be suppressed. The only compromise was that

Table 5
Final list of all three-dimensional numerical cavity flow simulations

Name	Turb. model	Pulse freq. (Hz)	Pulse amp. (V/U_∞)	Steady amp.	Grid
Base 1	k–ε	0.0	0.0	0.0	Coarse
Base 2	Hybrid	0.0	0.0	0.0	Coarse
Base 3	Hybrid	0.0	0.0	0.0	Fine
SJ1	Hybrid	0.0	0.0	1.02	Fine
LF1	Hybrid	271.0	1.67	0.0	Fine
MF2	Hybrid	556.0	1.67	0.0	Fine
MF1	Hybrid	1000.0	1.67	0.0	Fine
HF2	Hybrid	3000.0	1.67	0.0	Fine
HF3	Hybrid	4000.0	1.67	0.0	Fine
HF1	Hybrid	5000.0	1.67	0.0	Fine
HF1R	Hybrid	5000.0	1.07	0.0	Fine
HF1RS	Hybrid	5000.0	1.07	.366	Fine

the 1st mode was dominant at the time. Based upon how HF shear flow "stabilization" works, this is still an adequate demonstration of the efficacy of this flow control approach.

The first letters, "L", "M", "H", and "S", stand for low, mid-range, high, and steady, respectively. "F" stands for "frequency". The "R" in "HF1RS" stands for reduced mass flow rate.

Table 6 lists the differences between the current simulations, and the LES simulation of Rizzetta and Visbal [9]. The last two columns represent the ratio of the simulation value to the experimental value. This difference in pulsing amplitude and boundary-layer thickness plays a critical role in these types of simulations.

Fig. 12 shows the spectra for the two lowest frequency pulsing cases, LF1 (271 Hz), MF2 (556 Hz), as well as the steady injection case, SJ1. Included in the figure for comparison is the baseline case, BASE3, marked "fine, hybrid". The not unexpected result is that the LF type of forcing does not deliver effective suppression compared against the BASE3 case.

Fig. 13 shows a collection of spectra, meant to highlight the relative standing of the 1000 Hz (HF2) forcing case. It can be seen in this figure that although the HF2 case does provide at least 5 dB reduction of both the 1st and 2nd Rossiter modes (at roughly 250 and 500 Hz), it also creates a significant peak at the forcing frequency, which at least partially offsets any suppression benefit.

Fig. 14 shows the best numerical suppression case (HF2, 3000 Hz), plotted against several sets of experimental data. The HF2 case takes about 5 dB extra off the 2nd mode peak when compared against the spoiler. It still leaves about a 157 dB peak behind at 3000 Hz. Note again that since the calculation does not appear to be capturing the significant (about 10 dB) drop of the broadband shown in the experimental data for the resonance tube, it is possible that the peak left behind from the device could also drop another 10 dB if that effect was captured.

Table 6
Comparison between present conditions and LES of Rizzetta and Visbal [9]

Re_L	Mach number	Boundary-layer thickness wrt experiment	Flow control mass flow rate wrt experiment	
Present hybrid	7,230,000	1.2	1.0	1.00
Rizzetta et al. LES	200,000	1.2	2.0	0.64

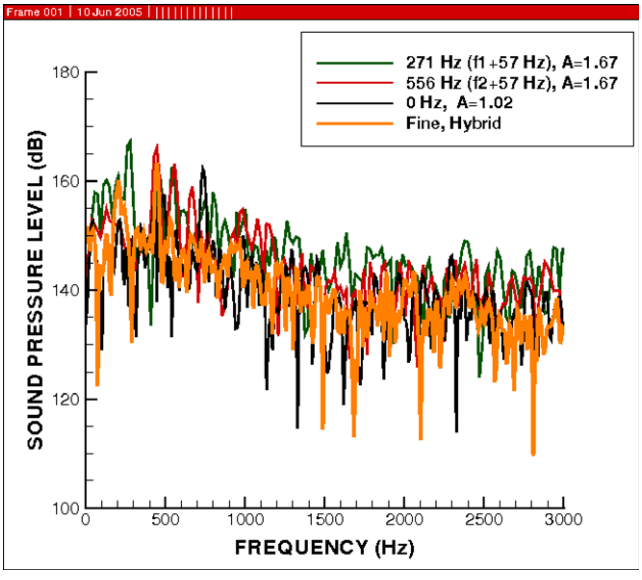

Fig. 12. Rear wall pressure spectra. Low frequency forcing & steady blowing.

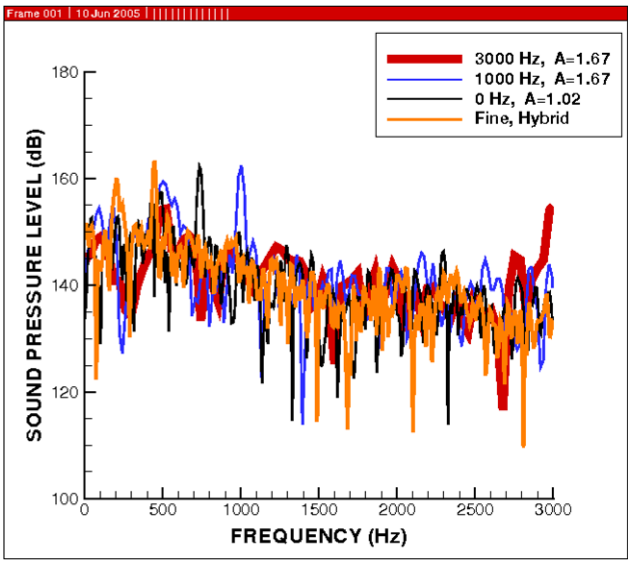

Fig. 13. Spectra highlighting relative standing of 1 kHz forcing case.

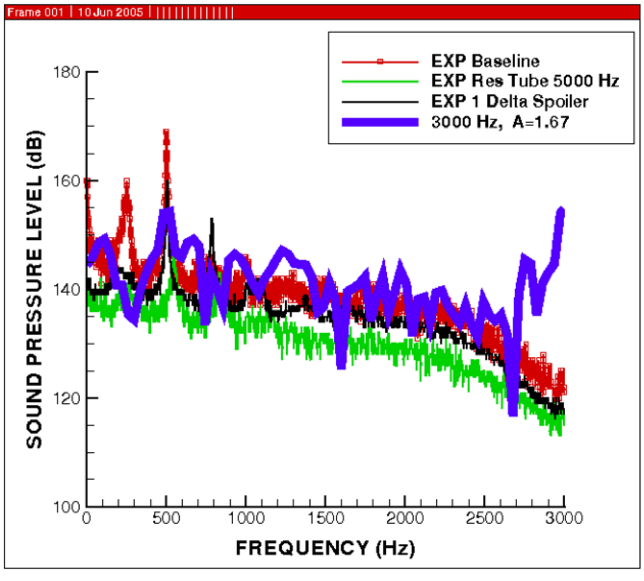

Fig. 14. Spectra of best numerical suppression vs. experimental data.

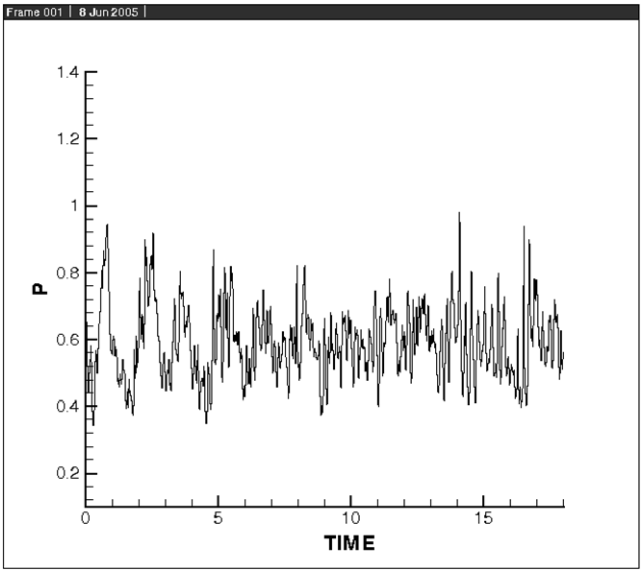

Fig. 15. Pressure history on rear wall, "HF2" – 3000 Hz, Amp = 1.67 (started from "MF1" solution, at time = 29.7).

Fig. 15 shows the rear wall pressure trace for the best suppression case (HF2, 3000 Hz), for comparison with the unsuppressed trace in Fig. 10. Spectra for all the cases described in this paper, as well as a more comprehensive description of these cases can be found in Ref. [15].

8.3. Evidence of a physical mechanism responsible for stabilizing a turbulent free shear layer

Fig. 16 shows time-averaged z component of vorticity contours for several of these hybrid RANS-LES cavity calculations, viewed from the top. The dramatic "V" shape in insets "d" and "e" are visible evidence of a spanwise instability and breakdown of the injected mass pulses (and created pair of vortices) as they travel downstream from the cavity leading edge. Fig. 17 shows the same view of time-averaged z component of the Reynolds stress $\overline{w'w'}$. It is obvious in insets "d" and "e" that the spanwise breakdown creates a dramatic change in this parameter not visible in insets "a", "b", "c", or "f".

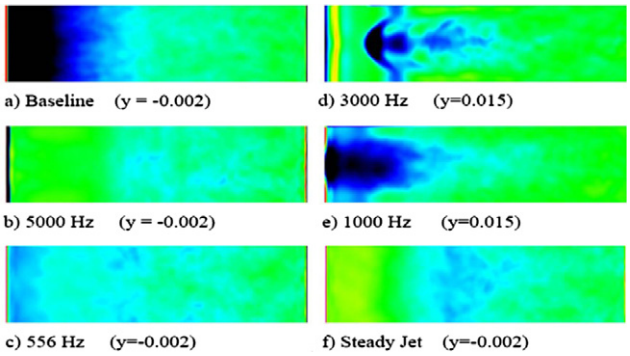

Fig. 16. Time-averaged z component of vorticity (constant y plane).

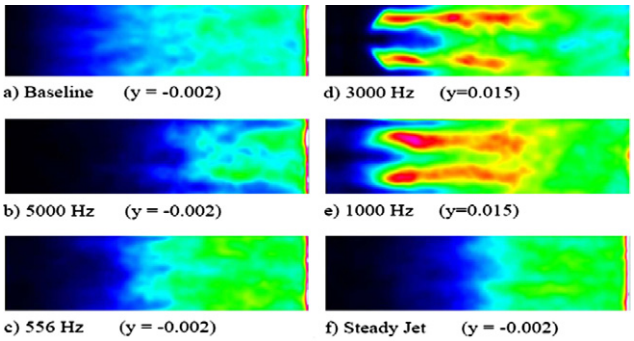

Fig. 17. Time-averaged z component of Reynolds stress $\overline{w'w'}$ (constant y plane).

Fig. 18 shows a similar instability and breakdown phenomenon from a simulation of a train of vortical structures created by a laminar jet next to a wall [23]. The strong, coherent vortical structures are shown to undergo a dramatic spanwise instability, leading to the same characteristic "V" shape seen in our cavity simulations. The instability is more dramatic and easier to see in this laminar wall jet case because the "starting" laminar vortices are pristine (not "turbulent" as in the cavity flow), and the breakdown process is much easier to visualize (the contrast between regions of laminar and turbulent flow is more stark). It is presented here for the sake of clarity of illustration.

Fig. 20 illustrates instantaneous contours of several quantities for the three most successful flow control cases with respect to suppression. Fig. 19 replaces one of those cases with a case which showed the strongest acoustic resonance (far right). What can be seen in these two figures is the breakdown in the spanwise direction of the injected vortex pair for cases with successful suppression (resulting in no coherent structure by the time the rear cavity wall is reached), vs. a case where no spanwise breakdown of the

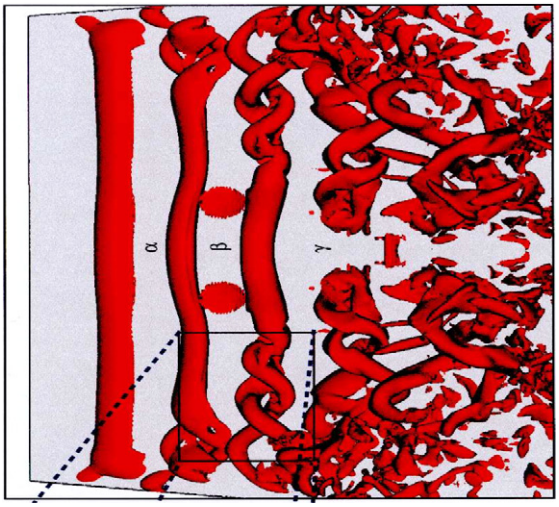

Fig. 18. Dramatic picture of a spanwise breakdown of coherent vortical structures as they travel from left to right. This was an initially laminar flow transitioning to turbulent flow. Used only to illustrate the nature of this type of breakdown [23].

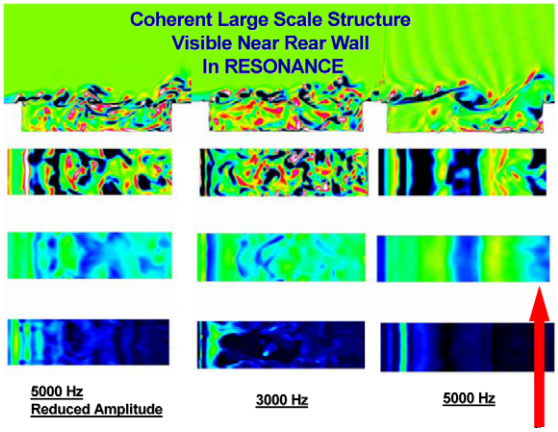

Fig. 19. Instantaneous flooded contours of (top to bottom) z component of vorticity, side view and top view, pressure coefficient, and eddy viscosity. Case on far right exhibits strong acoustic resonance. Coherent structure visible near rear wall.

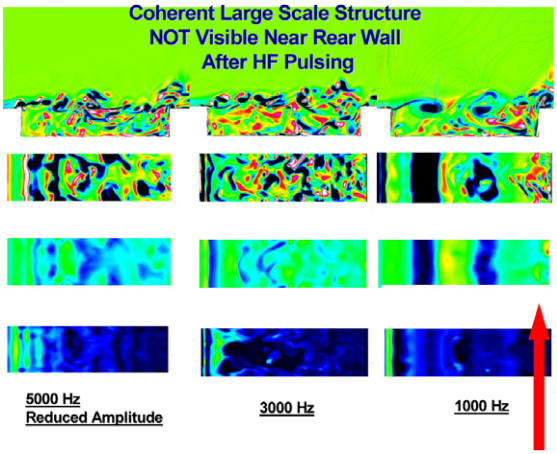

Fig. 20. Instantaneous flooded contours of (top to bottom) z component of vorticity, side view and top view, pressure coefficient, and eddy viscosity. Case on far right exhibits first signs of spanwise breakdown of vortex created by high frequency pulsing. No coherent structure is visible near rear wall.

injected pair occurred, no acoustic suppression occurred, and the injected vortex grew and remained coherent right up to the rear wall.

Fig. 21 shows a description of the sequence of steps which lead to the spanwise breakdown, and to the dramatic stabilization and control of the turbulent shear layer with successful HF pulsing.

The behavior observed in the entire series of cavity simulations (from steady mass injection, to LF pulsing, to HF pulsing) can be summarized in graphical form in Fig. 22. At low pulsed mass injection frequencies (in the vicinity of frequencies which the shear layer naturally amplifies), the injected pulsed mass encourages the formation of large ''rollers'' with strong spanwise coherence. The flowfield in this case is in a highly organized state, and the large-scale structures continue to grow and amplify as they travel downstream. But as the frequency is continually raised, a point is eventually reached where the injected structure is not encouraged to grow. Over a range of high frequencies, the injected structure ''self-destructs'', and in the process, not only does the injected structure not grow, but the flowfield is ''spoiled'' for the growth of any lower frequency structures as well. The specific conditions required for the ''self destruction'' of the vortical structures created during pulsing are described in Ref. [15].

Fig. 23 shows time-averaged fluctuating pressure contours for a collection of flow control and baseline cases. Inset ''d'' presents the lowest fluctuating pressure on the

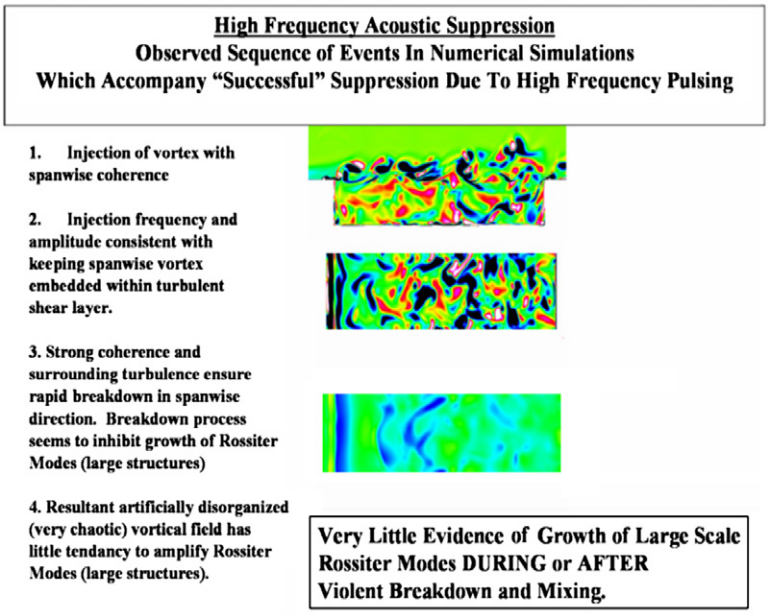

Fig. 21. Capsule description of observed sequence of events during high frequency pulsed flow control in cavity simulations [15].

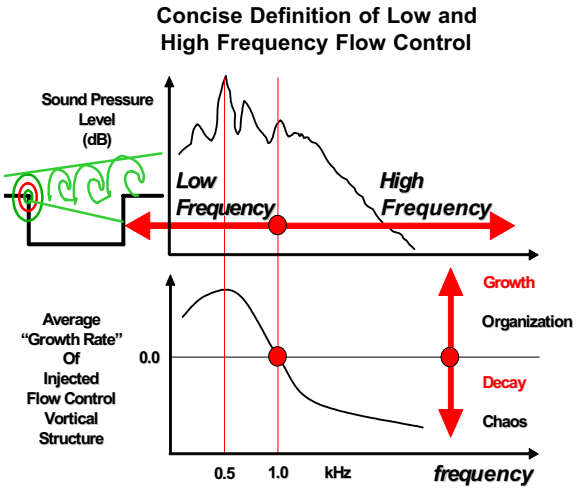

Fig. 22. Schematic capturing the behavior observed in cavity simulations as frequency of pulsed flow control is varied. Top inset represents typical pressure spectra showing energy levels at various frequencies (for an uncontrolled case). As the pulsing frequency goes up, the peaks or "tones" in the spectra are eventually suppressed. Change in growth rate from positive to negative represents definition of what "high frequency" is.

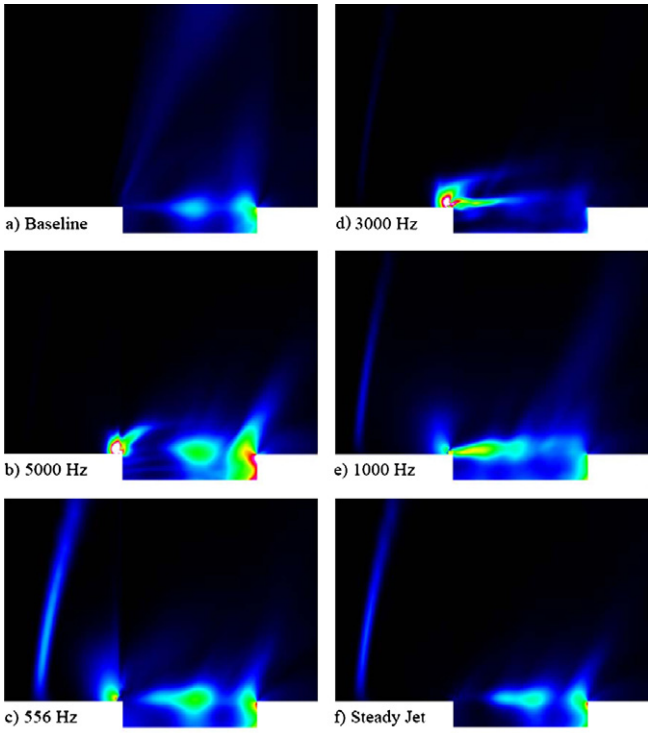

Fig. 23. Span-averaged, time-averaged fluctuating pressure correlation $\overline{p'p'}$.

back wall due to HF control at 3 kHz. Consistent with the lowest unsteady pressures for this case is a dramatic reduction in the LF undulation of the shear layer, and by a marked flattening of the averaged shear layer and reduction in the shear layer spreading rate (as seen in average u velocity contours). A comprehensive collection of time-averaged contour plots for a host of variables and cases is available in Ref. [15]

9. Other evidence of stabilization due to high frequency pulsing

The type of shear layer stabilization behavior evident in these cavity simulations is consistent with other available experimental and computational evidence concerning HF flow control in cavities [8]. Extensive experimental testing of the use of a rod in crossflow as a HF cavity actuator showed that the rod device (which sheds a train of alternating sign vortical structures similar to a pulsing jet) required an initially coherent spanwise structure for the stabilization (and acoustic suppression) to occur. Those results also showed loss of spanwise coherence of the initial HF vortical structures in the downstream direction (consistent with the behavior in the present cavity simulations). Subsequent experimental rod actuator testing in a different cavity configuration, where the rod was tested both with and without a "coherence spoiling helical strip" (similar to that seen on car antennas), showed that spoiling initial coherence of the rod shedding eliminated the dramatic suppression performance [38]. Although there is no visualization evidence (either experimental or computational) of spanwise breakdown behind rod actuators available in the literature, there is compelling secondary evidence to warrant speculation that it does happen in those cases. All available evidence shows that for successful HF shear layer stabilization the initial HF pulsed vortical structure must have spanwise coherence, and that this spanwise coherence is then lost as the structure breaks down while traveling in the downstream direction. A more detailed discussion of rod in crossflow experimental results is available in Ref. [15].

10. More fundamental arguments for stabilization of the turbulent shear layer

Earlier it was argued that previous numerical simulations of HF control in cavities did not offer insight into the mechanism of suppression. This was due to the fact that there was no description of the sequence of steps or events which led to the suppression. So far, the current results describe the initial requirement (creation of initially spanwise coherent injected structure), and the second step (violent spanwise breakdown). It is now useful to discuss the end result of those first two steps.

The violent breakdown of the pair of opposite sign vortical structures produced by (a) alternate side shedding from the rod, or (b) the upstream and downstream edge of the injected jet, leads to a dramatic reorganization of the vorticity field downstream. This reorganization can be examined from both an instantaneous and an averaged perspective. The averaged field is best described in terms of inviscid stability concepts (which is a macroscopic type of description), while the instantaneous field is best described from the viewpoint of the flowfield kinematics.

Stanek [39] discusses the fact that the modification of the turbulent vortical field can be described from either a macro and micro perspective. From the macro perspective (the stability of the mean flowfield), it can be seen that there is consistent behavior from both rod and pulsed jet HF control simulations.

Arunajatesan et al. [10] numerically simulated the rod in crossflow as a cavity flow control technique. Mean velocity profiles at a series of x locations are shown in the top of Fig. 24, before and after the use of the rod. The bottom of Fig. 24 shows a progression of mean velocity profiles from the current pulsed mass injection cavity studies. The changes in the mean velocity profiles due to the two different types of flow control are quite similar. Even though it is not described in Arunajatesan et al., it is likely that the introduction of a spanwise coherent structure in the Arunajatesan et al. simulation leads to the same type of spanwise breakdown seen in the current study. While no formal stability analysis has been performed for either of these two cases, it is clear from the profiles that a stability analysis would show a similar result (likely stabilization) in both cases. It is also obvious that the velocity profile changes induced by the HF flow control are quite dramatic, not subtle. This type of fluid dynamic stability analysis would constitute a macro-scale look at the effect of flow control on these shear layers.

There is obviously only one unique physical behavior resulting from the HF flow control, and the micro and macro views of that one behavior have to yield the same explanations or conclusions. Now we will look at the HF control (the coherent injected structure, breakdown, and resultant intense mixing) and try to see if there is a plausible explanation for why stabilization might occur from the micro-scale viewpoint.

Fig. 25, which is adapted from a figure and argument in the textbook by Sherman [40], is used to argue that an infinitely thin sheet of same sign vortex elements is unstable to any amplitude or frequency of disturbance – the so-called Kelvin Helmholtz instability. The reader is referred to Sherman [40] for the proof, which is based solely upon sim-

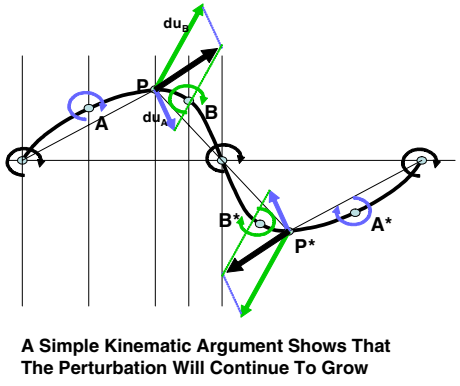

Fig. 25. Sketch used to prove infinitely thin vortex sheet is unconditionally unstable – using kinematic arguments.

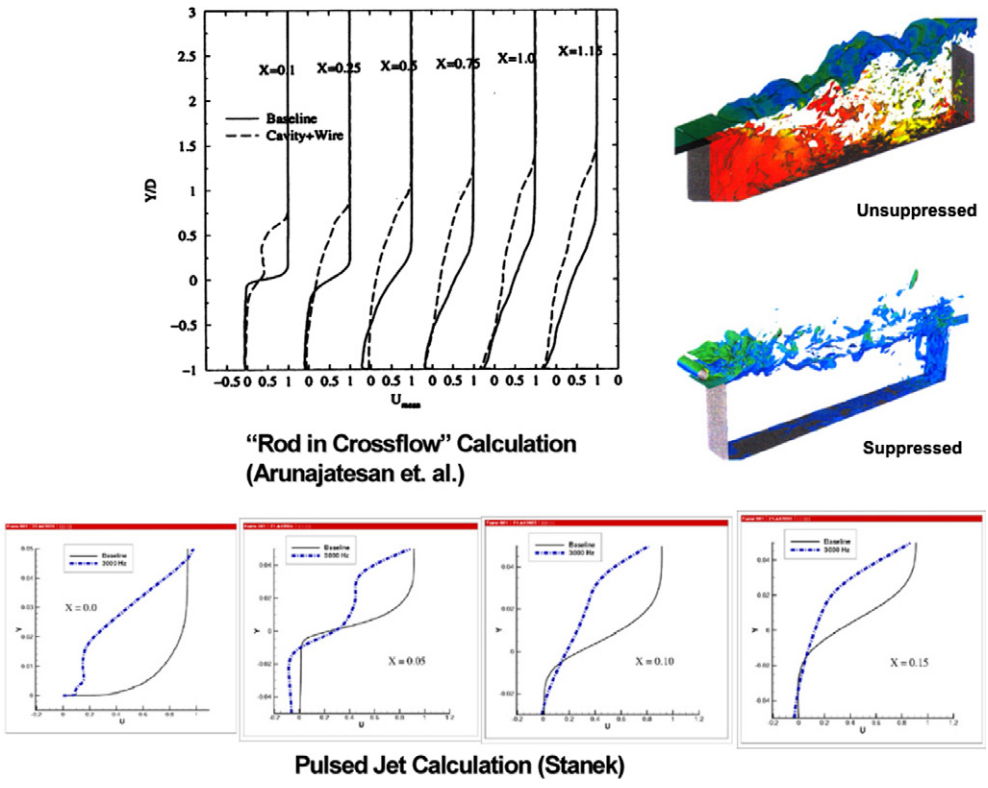

Fig. 24. "Before suppression" and "after suppression" mean velocity profiles as one travels downstream from the leading edge of the cavity. Profiles in top half of figure are from simulation of HF pulsing due to cylinder shedding. Similar profiles in bottom half of figure are from HF pulsed leading edge mass-addition simulations [15,10].

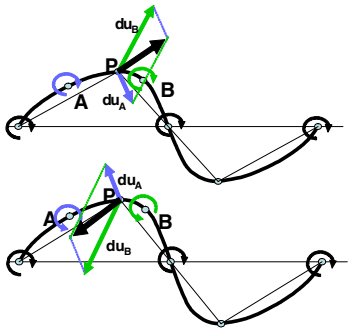

Fig. 26. Modification of Fig. 25. Replacing every other vortex with opposite sign dramatically stabilizes previously unstable situation – kinematic argument.

ple kinematic arguments. As a thought experiment, the reader is now asked to take the vortex elements in the first example (Fig. 25), and to replace half of them (every other one) with equal strength elements of the opposite sign (Fig. 26). If the reader goes through the same kinematic arguments as was used in the first example (again, see [40]), he will see that this new vorticity distribution is very stable to arbitrary perturbation, since adjacent elements now tend to cancel the effects of each other out, rather than reinforcing each other.

If we further extend the physical situation in our thought experiment (Fig. 26) to a finite thickness array of opposite sign, same size, vortex elements, and distribute them in a "plus, minus, plus, minus" fashion, we arrive at a situation shown in Fig. 27. By observation, the kinematics of this situation shows that elements within this finite layer are held in stasis, and the same alternating sign of the adjacent vortex elements shows the strong tendency to not amplify any arbitrary perturbations imposed upon this vorticity layer.

What we can conclude from these simple textbook-type arguments is that the movement from a "lattice" of same sign vortex elements, to a lattice of same strength "plus–minus" distributed vorticity is a movement from strong instability tendencies toward strong stability tendancies. In our "pre-flow control" turbulent cavity shear layer simulations, there are both signs of vorticity present, but the majority of the vorticity within the shear layer itself is of one sign. The reorganized vortex pattern within the shear layer after HF pulsing and violent breakdown and mixing, moves in the direction of a field of small sized, mixed positive and negative vortex elements, where no one sign is as dominant as before. If we fall back on our "textbook" example, we would suspect that the vorticity distribution after HF control is much more stable to LF disturbances, than the untreated vorticity distribution without HF control.

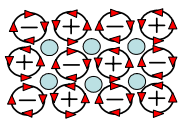

Fig. 27. Extending situation in Fig. 26 to shear layer of finite thickness – still very stable to disturbances.

11. Toward a mechanism

With the kinematic descriptions of the previous section in hand, one can come close to a description of mechanism for the class of HF devices (including rods and spanwise continuous HF pulsed jets) which produces a pair of initially spanwise coherent vortical structures. In simulation, this vortex pair interacts and produces a violent spanwise breakdown. The process of the breakdown and the field of vorticity left in the wake of this breakdown pushes the vorticity in the direction of a more random, less single-sign dominated field, and therefore towards stability. LF pulsing of the same shear layer does not lead to violent spanwise instability of the larger injected vortex pair, and does not reorganize the shear layer in any fundamental way. It simply perturbs the layer of single-sign dominated vorticity and encourages the layer to become unstable and roll-up into a large structure of the same sign as the free shear layer.

To the extent that the numerical simulations in the current study are physically realistic, this study constitutes proof that HF pulsing and LF pulsing are different types of shear layer control, dominated by distinctly different physics. The transition from one regime to the other is illustrated. The current study also, to the extent that the simulations are realistic, shows for the first time that the initial cause of the stabilization in HF control cases is the spanwise breakdown of the initial flow control structures. The kinematic arguments concerning the aftermath of the breakdown, while not proof per se, are satisfying nonetheless, because the readers can, if interested, make them themselves. Because the kinematic argument poses the problem of "given a certain pattern of particles and velocities, what happens in the next instant?", it represents a sequence forward in time – a step in the mechanism. Thus we are close to a step by step sequence, from the birth of the flow control pulse, to the breakdown, to the reorganization, to the instant after the reorganization, which amounts to a crude description of mechanism of stabilization of a turbulent shear layer.

12. Conclusions

The idea that pulsing a free shear layer (turbulent or laminar) could be used as a means to stabilization is one completely foreign to most practitioners of fluid dynamics. This is evidenced by the complete lack of discussion of the

topic in modern textbooks. It has recently been discovered, that it is indeed possible to temporarily stabilize the layer through a dramatic rearrangement of the vorticity in the layer. One reason that it is thought that this stabilization behavior has been hidden from view so long is that the actuators required for this effect must operate at both high frequency and high amplitude to achieve the required vorticity rearrangement- a difficult combination to achieve in practice.

The current work presents concrete evidence of the start of one possible HF mechanism (spanwise breakdown of the injected vortical structures), and provides two arguments for how this spanwise breakdown ultimately leads to stabilization (modification of the mean flow stability, and suppression of the natural "collective interaction" of the vortex elements normally present in the untreated shear layer). The spanwise breakdown mechanism illustrated in the current work, might of course, not be the only way to achieve stabilization through dramatic rearrangement of the vorticity field.

The current work, combined with supporting experimental evidence [8] demonstrates conclusively that the so-called "high frequency flow control" effect exists. This study does so by simulating an entire range of frequencies, and showing that the response of the turbulent free shear layer to pulsing dramatically changes above a certain critical frequency. It is also unique in that it is the first numerical study to demonstrate the critical role of spanwise instability to the success or failure of the HF control.

Experimental studies using rods in crossflow with cavities have shown that initial coherence of the injected HF structures is required for these devices to stabilize the shear layer. The current numerical study provides a critical missing link in that description by showing that the initial spanwise coherence allows for a dramatic spanwise breakdown and subsequent dramatic reorganization of the vorticity in the shear layer. It is this specific vorticity reorganization which is responsible for the observed stabilization. The experimental spoiled rod studies [38] combined with the current numerical study also shows that the mere presence of a particular dominant scale or frequency through pulsing is not a sufficient condition for stabilization – a resultant particular distribution of opposite signed (plus and minus) vorticity appears to be required as well. Essentially, the current study demonstrates the existence of so-called HF shear layer stabilization (and hence acoustic suppression) in high speed cavities by demonstrating what the mechanism is behind that stabilization.

Acknowledgements

This work was supported in part by a grant from the DoD HPC MSRC-ASC at WPAFB, OH. This work was presented at the ASME (American Society of Mechanical Engineering) Joint US – European Fluids Engineering Summer Meeting held in July 2006, in Miami, Florida.

References

[1] Panton RL. Incompressible flow. John Wiley and Sons; 1984. p 675.
[2] Nichols RH, Nelson CC. Weapons bay acoustic predictions using a multi-scale turbulence model. In: Proceedings of the ITEA 2001 aircraft-stores compatibility symposium, March 2001.
[3] Cattafesta LN, Williams D, Rowley C, Alvi F. Review of active control of flow-induced cavity resonance. ALAA Paper 2003-3567.
[4] Stanek MJ, Ross JA, Wrisdale I. High frequency acoustic suppression – experimental and computational overview. Paper No. 29, NATO RTO symposium on aging mechanisms and control, Manchester, UK, October 2001.
[5] McGrath S, Shaw L. Active control of shallow cavity acoustic resonance. AIAA Paper 96-1949.
[6] Stanek MJ, Raman G, Kibens V, Ross JA, Odedra J, Peto JW. Control of cavity resonance through very high frequency forcing. AIAA Paper 2000-1905.
[7] Stanek MJ, Raman G, Ross JA, Odedra J, Peto J, Alvi F, Kibens V. High frequency acoustic suppression – the role of mass flow, the notion of superposition, and the role of inviscid instability – a new model (Part II). AIAA Paper 2002-2404.
[8] Stanek MJ, Ross JA, Odedra J, Peto J. High frequency acoustic suppression – the mystery of the rod-in-crossflow revealed. AIAA Paper 2003-0007.
[9] Rizzetta DP, Visbal MR. Large-eddy simulation of supersonic cavity flowfields including flow control. AIAA Paper 2002-2853.
[10] Arunajatesan S, Shipman JD, Sinha N. Hybrid RANS-LES simulation of cavity flowfields with control. AIAA Paper 2002-1130.
[11] Tramel R, Rock S, Ellis J, Sharpes D. Comparison of large cavity aeroacoustic computations with flight test results. AIAA Paper 2005-2800.
[12] Das K, Hamed A, Basu D. Numerical investigations of transonic cavity flow control using steady and pulsed fluidic injection. ASME Paper FEDSM2005-77422.
[13] Gaitonde D, Visbal MR. High-order schemes for Navier–Stokes equations: algorithm and implementation into FDL3DI. AFRL-VA-WP-TR-1998-3060.
[14] Pulliam TH, Steger JL. Implicit finite difference simulation of three-dimensional compressible flows. AIAA J 1980;18(2):159–67.
[15] Stanek MJ. A numerical study of the effect of frequency of pulsed flow control applied to a rectangular cavity in supersonic crossflow. Ph.D. Thesis, University of Cincinnati, July, 2005.
[16] Beam RM, Warming RF. An implicit factored scheme for the compressible Navier–Stokes equations. AIAA J 1978;16(4):393–402.
[17] Jameson A, Schmidt W, Turkel E. Numerical solutions of the Euler equations by finite volume methods using Runge–Kutta time-stepping schemes. AIAA Paper 81-1259.
[18] Pulliam TH, Chaussee DS. A diagonal form of an implicit approximate-factorization algorithm. J Comput Phys 1981;39(2):347–63.
[19] Gordnier RE, Visbal MR. Numerical simulation of Delta-Wing roll. Aerospace Science and Technology 1998;2(6):347–57.
[20] Gordnier RE. Computation of Delta-Wing roll maneuvers. J Aircraft 1995;32(3):486–92.
[21] Visbal MR. Computational study of vortex breakdown on a pitching delta wing. AIAA Paper 93-2974.
[22] Visbal MR. Onset of vortex breakdown above a pitching delta wing. AIAA J 1994;32(8):1568–75.
[23] Visbal MR, Gaitonde DV, Gogineni SP. Direct numerical simulation of a forced transitional plane wall jet. AIAA Paper 1998-2643.
[24] Rizzetta DP, Visbal MR, Stanek MJ. Numerical investigation of synthetic jet flowfields. AIAA J 1999;37(8):919–27.

[25] Rizzetta DP, Visbal MR, Blaisdell GA. Application of a high-order compact difference scheme to large-eddy and direct numerical simulation. AIAA Paper 99-3714.
[26] Rizzetta DP, Visbal MR. Large-eddy simulation of supersonic compression ramp flows. AIAA Paper 2001-2858.
[27] Rizzetta DP, Visbal MR, Gaitonde DV. Large-eddy simulation of supersonic compression-ramp flow by a high-order method. AIAA J 2001;39(12):2283–92.
[28] Nichols RH, Nelson CC. Application of hybrid RANS-LES turbulence models. AIAA Paper 2003-0083.
[29] Jones WP, Launder BE. The prediction of laminarization with a two-equation model of turbulence. Int J Heat Mass Transfer 1972;15(2):301–14.
[30] Rizzetta DP. Numerical simulation of turbulent cylinder juncture flowfields. AIAA J 1994;32(6):1113–9.
[31] Hanjalic K, Launder B, Schiestel R. Multiple-time-scale concepts in turbulent shear flows. In: Bradbury LJS et al., editors. Turbulent shear flows, vol. 2. New York: Springer-Verlag; 1980. p. 36–49.
[32] Kim SW, Chen CP. A multiple-time-scale turbulence model based on variable partitioning of the turbulent kinetic energy spectrum. AIAA Paper 88-0221.
[33] Duncan B, Liou W. A multiple-scale turbulence model for incompressible flow. AIAA Paper 93-0086.
[34] Benek JA, Dougherty FC, Steger JL, Buning PG. Chimera: a grid-embedding technique. AEDC-TR-85-64, December 1985.
[35] Benek JA, Donegan TL, Suhs NE. Extended Chimera grid-embedding scheme with applications to viscous flows. AIAA Paper 87-1126, June 1987.
[36] Suhs NE, Rogers SE, Dietz WE. PEGASUS 5: an automated preprocessor for overset-grid CFD. AIAA Paper 2002-3186.
[37] Message Passing Interface Forum. MPI: a message-passing interface standard. Computer Science Department Technical Report, CS-94-230. University of Tennessee, Knoxville, TN, April 1994.
[38] Grove J. Private communication, April 2006.
[39] Stanek MJ. Control of high speed turbulent free shear flows – stabilization and destabilization. Keynote Lecture No. ICCES0520051003975, International conference on computational and experimental engineering and sciences (ICCES). Indian Institute of Technology Madras, Chennai, India, December, 2005.
[40] Sherman FS. Viscous flow. McGraw-Hill, Inc.; 1990.